Journal of Power Sources 483 (2021) 229108

Contents lists available at ScienceDirect

Journal of Power Sources

journal homepage: www.elsevier.com/locate/jpowsour

Data driven estimation of electric vehicle battery state-of-charge informed by automotive simulations and multi-physics modeling

Marco Ragone, Vitaliy Yurkiv, Ajaykrishna Ramasubramanian, Babak Kashir, Farzad Mashayek *

Department of Mechanical and Industrial Engineering, University of Illinois at Chicago, Chicago, IL, 60607, USA

HIGHLIGHTS

- Data driven algorithms used to predict the battery SOC in BEV applications.
- Modeling method implemented for generating realistic data of BEV driving behavior.
- Simulated formation/decomposition of SEI for modeling battery degradation.
- Tesla S and Nissan Leaf vehicles considered as case studies.

ARTICLE INFO

Keywords:
State-of-charge (SOC)
Battery electric vehicles (BEVs)
Automotive simulations
Electrochemical-thermal modeling
Machine learning (ML)
Deep learning (DL)

ABSTRACT

State-of-charge (SOC) estimation in a lithium-ion battery (LIB) is a crucial task of the battery management system (BMS) in battery electric vehicle (BEV) applications. In this work, we propose a modeling framework for SOC estimation using different machine learning (ML) methods, i.e. support vector regressor (SVR), artificial neural network (ANN), and long-short term memory (LSTM) network. The necessary training data have been developed using Matlab/Simulink automotive simulations of BEV, integrated with an electrochemical Comsol Multiphysics model of LIBs. The developed multi-physics model of BEV and LIBs operation allows to investigate the effect of driving conditions on the electrochemical and degradation (i.e., the solid electrolyte interphase – SEI – formation and decomposition) processes occurring inside batteries of different chemistries adopted in the Tesla S and Nissan Leaf BEVs. Our study remarks also the importance of taking into account the different components of BEV in the development of informative datasets, which are required for the implementation of learning algorithms for SOC evaluation. Thus, the proposed work establishes a basis for the generation of realistic training data based on simulations of BEV and LIBs dynamic response, which allows a more precise SOC estimation based on data-driven approaches.

1. Introduction

Global warming is recognized worldwide as one of the most critical challenges nowadays. The emission of tons of CO_2 gas during the operation of vehicles powered by internal combustion engines is one of the most harmful sources of environmental pollution in urban environments. To address these problems, the automotive industry is focusing more attention on electric vehicles [1], which are capable of integrating an electric motor as a propulsion system. Battery electric vehicles (BEVs) are particularly appealing due to the complete absence of a combustion engine and the usage of a battery pack as the primary energy source for the powertrain of the vehicle [2]. Nickel-metal hybrid (NiMH), nickel-cadmium (NiCd), lead-acid and lithium-ions (LIBs) are battery technologies typically adopted in automotive industry [3]. In particular, depending upon the chemistry, LIBs are capable of delivering high energy density or high power density and they have long lifetime and reduced cost compared to other technologies [4].

The functionality of LIBs in BEVs is dictated by the battery management system (BMS). The BMS is a collection of hardware (i.e., sensors, controllers, actuators, etc.) and software, which equips the battery pack in BEVs and it is responsible for enhancing its safety, protecting its individual cells from damage, increasing its efficient usage and

* Corresponding author.
E-mail address: mashayek@uic.edu (F. Mashayek).

https://doi.org/10.1016/j.jpowsour.2020.229108
Received 24 August 2020; Received in revised form 3 October 2020; Accepted 18 October 2020
Available online 17 November 2020
0378-7753/

extending its lifespan [5]. One of the main tasks of the BMS is to monitor the state-of-charge (SOC) and the state-of-health (SOH) of the battery pack and to provide immediate intervention in the case of abnormal behavior. The evaluation of the online SOC is a challenging task, mainly because of the non-linearities of the processes that characterize the electrochemical behavior of the battery.

Several methods have been developed for SOC estimation in BEVs and they can be divided into different categories [6–8] such as conventional methods, model-based estimations methods, adaptive filtering methods, non-linear observers and learning algorithms. Conventional methods include open-circuit voltage (OCV) [9], electromotive force (EMF) [10], Coulomb counting [11] and internal resistance [12]. Model-based estimation methods are categorized as equivalent circuit models (ECM) [13], reduced-order models (ROM) [14], state-space models [15], electrochemical models (EM) [16] and electrochemical impedance spectroscopy models (EISM) [17]. On the other hand, the adaptive filter algorithm methods, also known as Bayesian frameworks, include Kalman Filters (KF) [18], Extended Kalman Filters (EKF) [19], Unscented Kalman Filters (UKF) [20] and Adaptive Unscented Kalman Filters (AUKF) [21]. Other approaches are non-linear observers methods [22], bi-linear interpolation (BI) techniques and particle filter (PF) method [23]. Learning algorithms for SOC estimation such as fuzzy logic (FL) [24], genetic algorithm (GA) [25], and machine learning (ML) [26–35], form a special group of methods, since they do not involve parameters estimation, modeling of physical processes within the battery or its dynamic states. In fact, they exclusively rely on learning the non-linearities of the processes occurring within a cell through available training data of the battery characteristics (e.g., current, voltage and temperature) collected during laboratory tests. The state of knowledge of the application of ML models for battery's SOC estimation is further reviewed and analyzed Supplementary Information.

Despite the success in demonstrating the effectiveness of the data-driven models for the prediction of the SOC, the bottleneck of these approaches is that the data collected through laboratory experiments could not be fully representative of practical BEVs operation. First, the discharge is performed for few cells or even for a single cell, while a BEV is characterized by a battery pack comprising several modules of cells connected in series and in parallel. The full discharge of a cell in a laboratory results in a limited number of hours of operation, and it consequently turns into a reduced driving range compared to the distance that can be achieved by the BEVs currently used on the market. For example, the Environmental Protection Agency (EPA) estimated that the Tesla S model is capable to cover a distance of 391 miles (630 km) [36] before recharging the battery, while Nissan Leaf has a driving range of 226 miles (363 km) [37]. As a second reason, discharging a cell in a laboratory does not allow to take into account the characteristics of other components of the vehicle such as the electric motor, the power-train system or external conditions like the aerodynamic resistance of the air, which are dynamically coupled with the battery pack in the operation of the BEV and they consequently impact the discharge of the cell. Last but not least, in almost all the works reported in the prior literature, the data are collected from single cell chemistry. Since the relationship between the SOC and the battery characteristics is highly dependent on the electrochemical process and the reactions occurring inside the cell, a model trained on data obtained from particular chemistry cannot be able to predict accurately the SOC of a cell for a different chemistry and training should be repeated.

In order to address these challenges, in this work we propose a multi-physics modeling framework to generate realistic training data for learning-based techniques applied to SOC estimation in BEVs. The developed model of BEV allows to compute the battery characteristics and a SOC with a high level of fidelity to practical driving conditions. Additional variables including the temporal variation of the mechanical power delivered by the electric motor and the power loss due to the aerodynamic resistance of the air are combined with the traditionally used electric current, voltage, and temperature to predict the SOC. The method has been applied to the Tesla S and Nissan Leaf models available in the BEV market, in order to obtain data reflecting up-to-date applications. Modeling the different chemistries of the cells characterizing the battery packs of the two vehicles (i.e., Nickel–Manganese–Cobalt and Lithium–Manganese-Oxide cathode materials) and the different operation of the electric motors and powertrain systems allows to generate a more informative dataset for training a data-driven model applied to BEVs. The US06, Federal Test Procedure 75 (FTP75), Heavy Duty Urban Dynamometer Driving Schedule (HDUDDS), Highway Fuel Economy Test (HWFET), Supplementary Federal Test Procedure (SC03) and Los Angeles 92 (LA92) are the driving cycles (DCs) used to simulate the different driving patterns for the collection of the dataset. Then, the generated data are adopted to train and test a support vector regressor (SVR), an artificial neural network (ANN), and a long short-term memory (LSTM) network, which are the most effective learning models adopted in the prior literature for the final SOC estimation.

In addition to the generation of data to be adopted in learning algorithms for SOC estimation, our study involves a numerical analysis of the degradation of the capacity of the battery during the BEVs operation, where formation/decomposition of the solid electrolyte interphase (SEI) is considered as a possible source of degradation. For this purpose, we have developed an electrochemical model for the cylindrical and pouch cells used in Tesla S and Nissan Leaf battery packs, where the discharge is simulated by applying the current computed through the automotive simulations. The growth of the SEI film has been monitored in the simulations. In this way, it is possible to explore how the BEV operation affects the degradation of the battery, which is one of the most serious challenges to be addressed in order to improve the performance of the existing battery pack in BEV.

2. Model description

The computational approach proposed in this work to investigate the battery SOC in BEVs combines automotive simulations, multi-physics electrochemical and thermal model of LIBs and ML models. Automotive simulations have been performed using the Matlab/Simulink platform [39]. The Matlab/Simulink library called Powertrain Blockset [40], which allows to build data-driven models of automotive powertrains such as gasoline, diesel and electric systems, is used. The main advantage of using blocks implemented in the Powertrain Blockset library is the customization of the parameters of the vehicle's components using appropriate look-up tables. In our problem, the blocks have been parametrized considering the technical specifications of Tesla S and Nissan Leaf models available in the Tesla and Nissan websites [36,37].

The battery degradation has been investigated using an electrochemical–thermal model of LIBs built in Comsol Multiphysics [41]. Comsol Multiphysics is well suited for the investigation of battery degradation since it incorporates dedicated libraries which allow to simulate the effect of electrochemical parameters such as the size of the particles of the electrode materials and the phases concentrations in the active materials and phenomena such as the charge transfer reactions at the interfaces between the electrodes and the electrolyte. The LIBs modeling in Comsol Multiphysics has been also used to generate the lookup tables for the parametrization of the battery block in the Matlab/Simulink model of the BEV.

Then, using the data generated through the BEVs automotive simulations, we have trained and tested an SVR, an ANN and an LSTM network on our augmented dataset comprising the characteristics of the BEVs' components. The implementation of the learning algorithms has been performed using the Scikit-Learn [42] and TensorFlow [43] libraries for ML and Deep Learning (DL) model development. The workflow of the presented modeling framework is illustrated in Fig. 1.

2.1. Automotive simulations

Herein, the technical description of the automotive simulations of

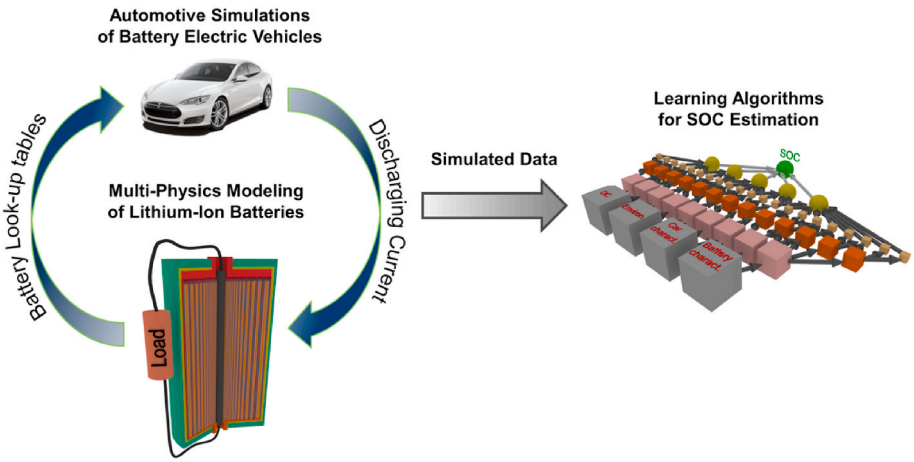

Fig. 1. Workflow of the modeling framework presented in this work. Automotive simulations of BEV combined with multi-physics modeling of LIBs have been used to generate the proper training data for the estimation of the SOC using ML algorithms. Training data reflect the DC, the environmental conditions, and realistic car's and battery's characteristics.

BEV implemented in Matlab/Simulink is reported. The model simulates the dynamic behavior of the battery pack, the electric motor, the differential, the wheels and brakes system and the vehicle body with dedicated blocks from the Powertrain Blockset library. A more detailed description of each module is provided in Supplementary Information (section 2), while only a brief summary is presented here.

The battery pack is implemented using the Datasheet Battery block [44], which uses an ECM with parameters estimated through look-up tables built by interpolating the discharge curves of the cells at constant C-rates and constant temperatures. Specifically, the discharge curves at different C-rates of 1C, 2C, 3C, 4C and 5C at a constant temperature of 293 K, and different temperatures of 263 K, 273 K, 293 K, 313 K at the constant 1C have been simulated using the developed electrochemical–thermal model in Comsol Multiphysics. We have considered the different characteristics of the cells adopted in the Tesla S and Nissan Leaf vehicles (i.e., cylindrical NMC 18650 cell and pouch LMO cell with a nominal capacity of 2.86 A h and 56.3 A h respectively). The Datasheet Battery block is implemented to take into account the series-parallel connections characterizing the battery packs of Tesla S (i.e., 96s86p) and Nissan Leaf (i.e., 96s3p). In this way, it is possible to simulate the discharge of the full battery packs of the two vehicles with a total energy of 100 kWh and 62 kWh, respectively. The block calculates the SOC using the Coulomb counting method.

The permanent magnet synchronous motor (PMSM) of Tesla S and Nissan Leaf is simulated using the Mapped Motor block [45]. The block controls the output shaft torque T_{shaft} to match the reference torque demand $T_{\text{reference demand}}$. The shaft torque T_{shaft} is computed through the characteristic curves of the motor at the specific angular speed.FX The reference torque $T_{\text{reference demand}}$ takes into account the positive torque needed during the acceleration of the vehicle $T_{\text{acceleration}}$ and the breaking torque $T_{\text{regenarative breaking}}$ responsible for the recuperation of the SOC during deceleration. The acceleration torque is obtained from the characteristic curve of the motor at the angular speed FX, and it is multiplied by the percentual acceleration $a_{[\%]}$ computed by the Proportional Integral (PI) controller to match the demand of the driving cycle.

The powertrain system of the vehicle is simulated by the Limited Slip Differential [46] and the Longitudinal Wheel [47] blocks, which compute the torque corresponding to the left and right axles (i.e., $T_{\text{left axle}}$ and $T_{\text{right axle}}$) and the net longitudinal forces applied to the rear and front wheels (i.e., $F_{\text{rear,x}}$ and $F_{\text{front,x}}$). The friction between the wheels and the tarmac is also considered. The dynamic of the vehicle is simulated using the Vehicle Body 1DOF Longitudinal [48] block. The block models the vehicle as one degree-of-freedom rigid body in longitudinal motion parallel to the ground, by taking into account the net longitudinal forces applied to the wheels and the aerodynamic drag force F_{drag} applied to the windshield due to the aerodynamic resistance of the air. The balance of forces involving the mass of the vehicle m_{vehichle}allows us to compute the acceleration $a_{\text{feedback}}$and then the resulting speed s_{feedback}. The feedback speed s_{feedback} is dynamically controlled by the PI controller to match the reference speed $s_{\text{reference}}$ of the applied DC.

A more detailed explanation of the construction of the look-up tables and differential equations characterizing each block is provided in the Mathworks websites dedicated to the Powertrain Blockset modules [40]. A schematic of the BEV model is illustrated in Fig. 2.

2.2. Multi-physics electrochemical and thermal modeling of lithium-ion battery

The objective of the multi-physics model is to characterize the electro-thermal behavior of the battery during BEV's operation taking into account the degradation phenomena due to the SEI formation. The finite element method (FEM) is used to simulate the cylindrical (Tesla S) and pouch (Nissan Leaf) cells, with a P2D model [49] including a degradation sub-model due to the SEI formation/decomposition [50,51], combined with a 3D thermal model to compute heat propagation within the cells. Here, we describe the P2D electrochemical, the degradation and the thermal models implemented in Comsol Multiphysics.

The P2D model describes the so-called repeat unit consisting of the two current collectors (both negative and positive), a negative electrode, electrolyte and positive electrode. Since the electrochemical model is described in the prior literature only an overview is given here. The cell model is based on a 1D continuum description of reaction and transport along electrodes, electrolyte and current collectors, plus an additional dimension in the electrode particle (P2D) [49]. Electrochemical charge-transfer reactions only occur at the interfaces of the electrodes and the electrolyte and are modeled using the Butler-Volmer equation [49].

The ionic charge balances and material balance in the electrolyte are modeled according to the equations for binary electrolytes. Electrons transport is not explicitly modeled due to the fast delivery to the current collector in comparison to the other processes in the battery. We use a homogenization approach (the Bruggeman relation) to model the transport properties in the porous electrode. Detailed definitions of symbols and additional equations for local current densities and voltage are given elsewhere [49].

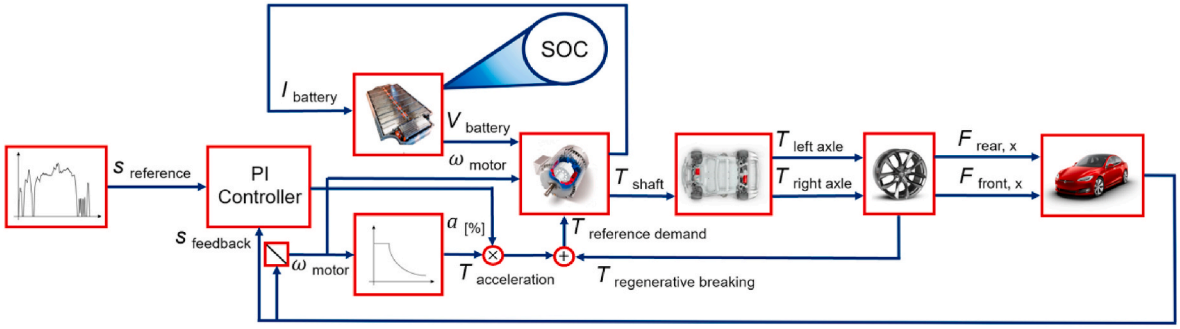

Fig. 2. Schematic of the BEV model built in Matlab/Simulink using dedicated blocks from the Powertrain Blockset library. The model takes as input a driving cycle which dictates the reference speed of the vehicle $s_{\text{reference}}$ and it simulates the dynamic of the BEV driving and it calculates the corresponding SOC variation.

The degradation model is used to simulate the behavior of the SEI during the BEV's operation. The SEI is used in the model to simulate the increase of the potential losses due to the resistance of the growing film on the electrode's particles. In addition, the electrolyte charge transport as a result of the reduction of the electrolyte volume fraction due to the SEI is considered. The SEI formation/decomposition is modeled using the parasitic current forming during this process and it is described by the following equation [52]:

$$i_{\text{loc,SE}_\text{I}} = -(1+\text{GE})\frac{J_{\text{exc}} i_{\text{loc,C,ref}}}{\exp\left(\frac{\alpha\eta_{\text{SEI}}F}{RT}\right)+\frac{q_{\text{SEI}}fJ_{\text{exc}}}{i_{\text{loc,C,ref}}}}, \tag{1}$$

where, $i_{\text{loc,C,ref}}$ is the local current density at particular C-rate, GE is a dimensionless graphite expansion factor, J_{exc} is dimensionless exchange current density for the parasitic reaction, α is the transfer coefficient of the electrochemical reduction reaction, η is the overpotential, q_{SEI} is the local accumulated charge due to the SEI formation, and f is a lumped nondimensional parameter based on the properties of the SEI film.

The thermal model simulates the heat generation and propagation within the cell. The generation of heat inside the battery is mainly triggered by charge transport and (electro-)chemical reactions during charge/discharge cycles [53]. The contributions to the heat losses within the cell are classified as irreversible due to the charge transfer reactions, reversible due the entropic changes during the lithium intercalation and Ohmic due to the current conduction in the solid and electrolyte phases. Thus, the energy conservation law is:

$$\rho^{\text{l}} C_p^{\text{l}} \frac{\partial T}{\partial t} = k_{\text{in}}^{\text{l}} \frac{\partial^2 T}{\partial x^2} + k_{\text{in}}^{\text{l}} \frac{\partial^2 T}{\partial y^2} + k_{\text{th}}^{\text{l}} \frac{\partial^2 T}{\partial z^2} + Q_{\text{irr}}^{\text{l}} + Q_{\text{rev}}^{\text{l}} + Q_{\text{ohm}}^{\text{l}}, \tag{2}$$

where ρ is the density of materials; C_p is the specific heat capacity, and k_{in} and k_{th} are the in-plane and through-plane thermal conductivity coefficients. The superscript 'l' in Eq. (2) indicates layer-specific properties. The last three terms in Eq. (2) define different heat generation mechanisms as described above (irreversible, reversible and ohmic). The details of these heat sources are given in Refs. [54,55]. The boundary condition for Eq. (2) is the convective heat transport through all the surfaces facing the ambient environment. In this way it is possible to model the cooling system present in the battery pack of the BEV, which is paramount to keep the temperature of the cells within the operating range of 298–312 K (25–40 °C). The thermal model is directly coupled to electrochemical and degradation sub-models and solved iteratively.

2.3. Machine learning models

The modeling data developed with the combined automotive and electrochemical models of BEV and LIBs described in the previous sections, have been used to train and test different ML models for the prediction of the battery's SOC. Here, we first introduce the variables used as input (features). Then, we briefly present the learning models we have selected for the estimation of the SOC.

The variables characterizing the battery are the discharging current, the voltage, the temperature and the SOC. The current, voltage and SOC variation is calculated by the battery block of the BEV model, while the temperature profile is computed by the thermal model of the cell. The powertrain of the system is included in the dataset considering the mechanical power delivered by the electric motor FX, the mechanical power transferred through the differential FX, the mechanical power transferred from the axles to the wheels FX, the mechanical power loss due to the rolling resistance FXand the mechanical power required for breaking the vehicle FX. Finally, we have considered the power loss due to the aerodynamic resistance of the wind. As a result, the time series of nine variables characterizing the vehicle operation have been combined to estimate the SOC. Adding the data related to the variation of the characteristics of each block provides a more comprehensive characterization of the vehicle dynamic and more informative dataset in respect to the case of using only the variables related to the battery cell (i.e., current, voltage and temperature). We have considered the learning algorithms belonging to the different categories described in section 2: SVR [26], ANN [28] and LSTM models [35]. Since an extensive description of SVR, ANN and LSTM models is reported in the literature, including reports regarding the application of these models in the estimation of SOC in BEV [34,38,43] only a brief summary is reported here.

SVR is the counterpart of the Support Vector Machine (SVM) classifier for the regression purpose. SVR predicts a target variable using a regression curve built upon an appropriate hyperplane, computed through a kernelized combination of the input variables. The linear kernel, the Gaussian kernel defined by the Radial Basis Function (RBF), the polynomial kernel of a predefined degree and Sigmoid kernel are typically used in SVM and SVR models. The data points which lie inside a hyperplane margin of a controlled width are called support vectors, and they are responsible for the final estimation of the target. The width of the margin is controlled by the hyperparameters comprising a regularization parameter C and a penalty slack variable ξ. The different kernels and values of the hyperparameters have been investigated using cross-validation to optimize the prediction of the SOC.

An ANN decomposes the relationships between the input variables and a target through a sequence of algebraic linear combinations built upon a deep architecture of so-called hidden layers comprising several activated neurons. The input variables and the target represent the input and the output layers of the network. The coefficients of the linear combinations are called weights and bias and they are calculated through an iterative optimization process based on the backpropagation and gradient descent algorithms. In our problem, we have adopted an ANN characterized by an input layer comprising nine neurons representing values of the nine input variables at a specific time t^*, with hidden layer and neurons activated by the Rectified Linear Unit (ReLu) activation function and an output layer with a single neuron for the final SOC prediction (Fig. 3a). The proper number of hidden layers and

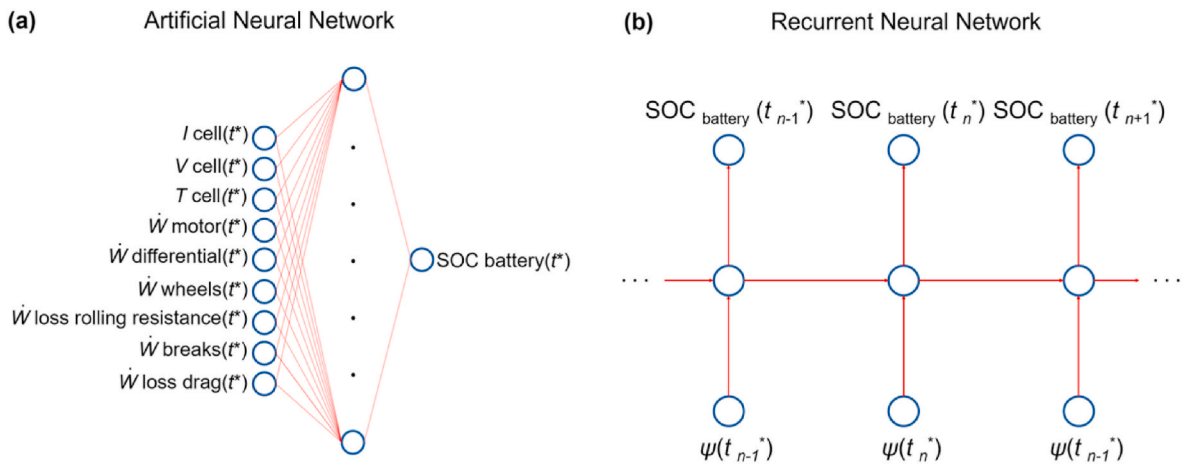

Fig. 3. Artificial Neural Network and Recurrent Neural Network for SOC estimation. The ANN takes as inputs the values of the variables characterizing the dynamic of the BEV computed at each time t^* from the automotive simulation. The target variable is the value of the SOC at the timet^*. **(a)** The RNN is built by combining many deep neural networks for each time t^*. **(b)** The sequence of l observations [FX, …,FX,FX] is used to predict the SOC at the time t_n^*.

neurons, as well as the number of iterations of the learning process, have been selected to optimize the SOC estimation. The Adam optimizer and the mean squared error (MSE) loss function have been used to compile the ANN model.

LSTM belongs to the RNN class of DL models designed for the estimation of time series with recurrences. An RNN model predicts the value of the target at a specific time step by considering the data belonging to a prior time sequence of a given temporal length l. The time series estimation is performed by constructing a deep network where multiple ANNs are built for each single time step of the sequence and concatenated to each other. The hidden layers of every single ANN are referred as hidden states of the RNN. LSTM is an optimized RNN, developed to address the vanishing gradient problem of standard RNN. LSTM combines the hidden states of the RNN with dedicated layers called cell states able to filter the non-useful information for the target prediction from the so-called short memory (close in time to the target) and the long memory (far in time from the target) of the network. In our problem, the values of the nine variables FX in the time sequence $[t^*_{n-l}, \dots t^*_{n-2}, t^*_{n-1}]$ of length l up to the time t^*_{n-1} are used to predict the SOC at the time t^*_n (Fig. 3b). Similar to ANN, the Adam optimizer and the MSE loss function has been used to compile the LSTM network. As in the case of SVR and ANN, the hyperparameters of the model (the length l of the time sequence and the optimal architecture of the LSTM network) have been investigated to find the most accurate SOC prediction.

Finally, the performance of the models has been evaluated by considering the MSE between the estimated and the true SOC, which is a metric typically used in regression problems:

$$MSE = \frac{\sum_{i=1}^{N} \left(SOC_{true,i} - SOC_{predicted,i}\right)^2}{N} \tag{3}$$

$N$is the total number of data points in the dataset, while $SOC_{true,i}$ and $SOC_{predicted,i}$ are the true and the predicted values of the SOC for the sample i.

3. Results and discussion

In this section, we present as first the development of the simulated data. Then, we illustrate the simulations of the SOC decay in BEV as a result of the SEI degradation. Finally, we report the prediction of the SOC using ML models trained and test on the modeling data.

3.1. Automotive simulations and datasets creation

We illustrate here the computed profiles of the variables characterizing the operation of the BEV, modeled using our proposed multi-physics approach. The BEV automotive simulations are performed considering several repetitions of the six DCs US06, FTP75, HDUDDS, HWFET, SC03 and LA92 for both the Tesla S and Nissan Leaf models. Using many DCs allows us to model different driving patterns and to provide a broader set of configurations for a data-driven model. For example, US06 driving cycle represents an aggressive and high speed/acceleration driving behavior with rapid speed fluctuations. On the other hand, HWFET has been developed to estimate the highway fuel economy rating, while FTP75 measures emissions in urban environments.

For each driving cycle, the number of repetitions is considered according to the EPA driving range for Tesla S and Nissan Leaf which are 391 miles (630 km) and 226 miles (363 km), respectively. In this way, it is possible to simulate the whole driving period before the battery pack needs to be recharged. The reliability of our automotive modeling is tested by evaluating the battery SOC drop: if the battery is empty (SOC consistently below 10%) at the end of the simulation when the maximum driving range is achieved, it means that the automotive model is reliable in representing the driving conditions of the two vehicles. For all the applied driving cycles, the SOC drops to values between 4% and 8% approximately, thus we consider that our BEV model is accurate in simulating the Tesla S and Nissan Leaf driving conditions. A time step of 1 s is considered, meaning that the number of datapoints simulated for a specific driving cycle is equal to the time in seconds required to discharge the battery. For all the cases, the simulations are performed at a constant ambient temperature of 298 K (25 °C). However, our BEV model is amenable to different values of the input environmental temperature, since the battery block has been parametrized using discharge curves at constant temperatures in the range 253K–313K, as shown in Figure S1 in Supplementary Information. In Figure S2 of Supplementary Information we have included the profiles of the SOC, the voltage and the applied current for environmental temperatures of 253K, 298K and 313K. For brevity, we report here only the results obtained by applying the FTP75 driving cycle.

Fig. 4 shows the discharge profiles simulated for the FTP75 driving cycle. As it is illustrated, the discharge curves for the two vehicles are different. Fig. 4b shows that the Nissan Leaf battery pack is discharged in approximately 11 h, while Tesla S can be driven for approximately 18 h following the FTP75 speed profile. The shapes of the voltage profiles shown in Fig. 4c are different because of the electrochemical behavior of

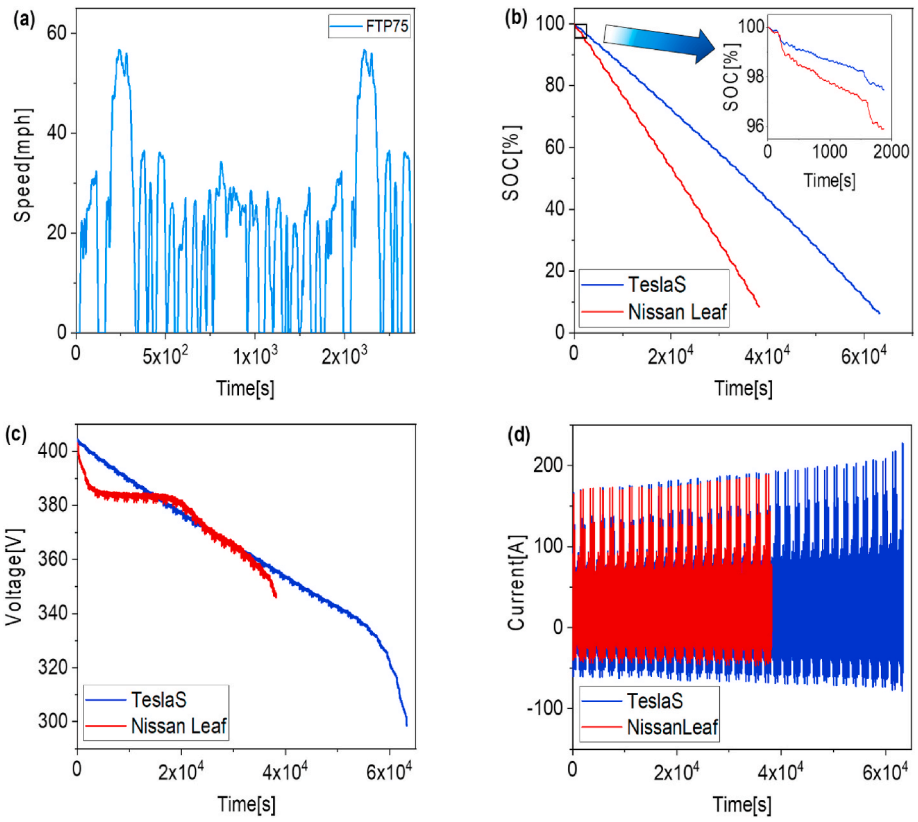

Fig. 4. Discharge characteristics simulated by applying the FTP75 driving cycle. **(a)** Speed profile of the FTP75 driving cycle. **(b)** Battery SOC with a zoom-in on the first repetition of FTP75 for the Tesla S and Nissan Leaf BEV models. **(c)** Discharging voltage and **(d)** discharging current for the Tesla S and Nissan Leaf BEV models.

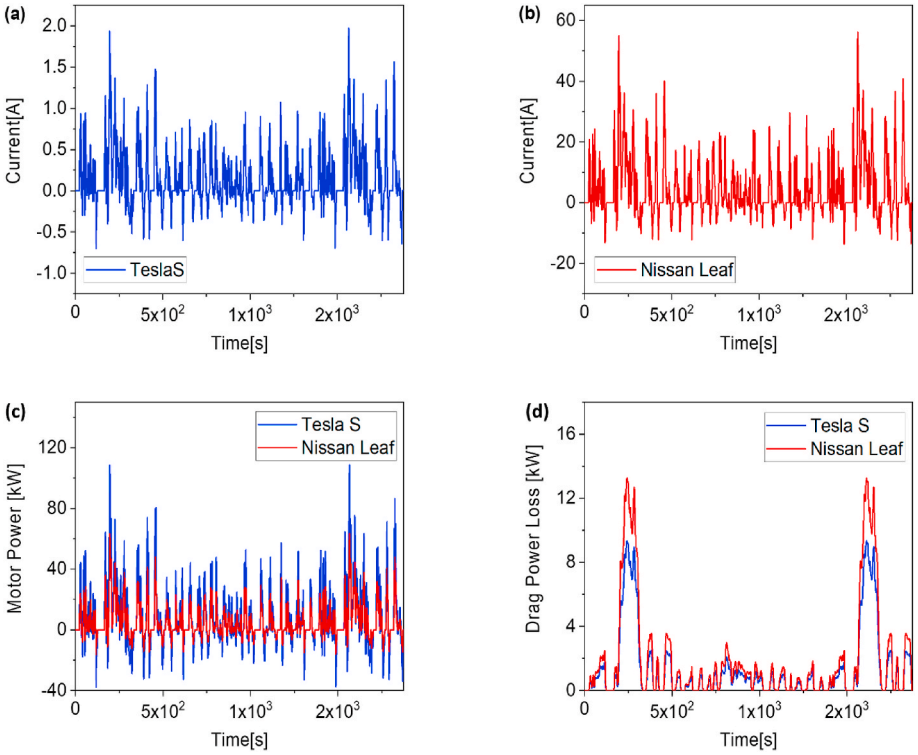

Fig. 5. Discharging current for a single repetition of the FTP75 driving cycle for **(a)** a cylindrical NMC cell of Tesla S battery pack and **(b)** a LMO pouch cell of Nissan Leaf battery pack. **(c)** Profile of the mechanical power, FX, delivered by the electric motor and **(d)** the power loss, FX, due to the aerodynamic resistance of the air during the first repetition of the FTP75 driving cycle.

the NMC cylindrical cells and LMO pouch cells characterizing the battery packs of the two vehicles. The discharging current of the Tesla S and Nissan Leaf presented in Fig. 4d overlap since the current profile is dictated by the acceleration, which depends exclusively on the profile of the applied driving cycle that is the same in the two cases. Tesla S has a slightly higher regenerative current (negative values of the current profile) since the torque responsible for the SOC recuperation depends on the characteristics of the powertrain system which is different in the two vehicles. However, the current flowing in each single cell of the battery pack is very different for the two vehicles. Since the number of groups of cells wired in parallel is 86 and 3 for the battery packs of Tesla S and Nissan Leaf, respectively, a less intense current flows through a Tesla S cell compared to Nissan Leaf.

Fig. 5a and **b** illustrate the cell's current profile for a single repetition of the FTP75 driving cycle for the two distinct cases of TeslaS and Nissan Leaf. The values of the cell's discharging current are obtained by dividing the current profile shown in Fig. 4d by the number of groups of cells in parallel.

In Fig. 5c and d, the profiles of the mechanical power delivered by the electric motor FX and the power losses due to the aerodynamic resistance of the air, FX, are illustrated. The profiles for the two vehicles vary due to the differences in technical characteristics of each component. The power delivered by Tesla S motor is higher compared to Nissan Leaf because the torque reported in the characteristic curve of Tesla S is more intense than the torque offered by Nissan Leaf (i.e., 660 Nm vs. 340 Nm) in the operating window of the angular speed corresponding to the driving conditions. Similarly, the power loss, FX, of Nissan Leaf slightly exceeds Tesla S because of the more extended surface of the windshield (i.e., 2.58 m^2 for Nissan Leaf and 2.34 m^2 for Tesla S) and the higher drag coefficient (i.e., 0.28 for Nissan Leaf and 0.24 for Tesla S). Since differences are present in the profiles related to the powertrain systems of the two vehicles, it is important to take them into account in training a data driven model for the prediction of the SOC.

The SOC is highly dependent on the operating temperature of the cell. In the prior literature, the temperature data are collected using thermocouples placed in contact with the cell [30]. Although this approach is the most straightforward in the acquisition of experimental data, it allows the user to record only the surface temperature of the cell, which is always lower compared to the bulk region. In particular, due to a large cell area, the surface of the cell is thermally stable during the discharge, so the experimental data do not allow to fully capture the temperature differences that exist between the cases of a sudden acceleration (high C-rate) of the vehicle to a high driving speed and a slower and stable (low C-rate) driving behavior. The modeling approach proposed in this work allows to simulate the temperature distribution within the core of the cylindrical NMC and pouch LMO cells of Tesla S and Nissan Leaf when a current demand corresponding to a DC is applied. In addition, the thermal model allows also to simulate the effect of the convective cooling adopted by the thermal management system of the BEV to control the temperature of the battery pack. The variation in time of the average temperature of the cylindrical NMC cell during the first iteration of the FTP75 driving cycle is shown in Fig. 6a, whereas Fig. 6b illustrates the contours of the temperature corresponding to four different levels of current demand (low demand at $t = 100$ s, high demand at $t = 200$ s, moderate demand at $t = 260$ s, intermediate demand at $t = 360$ s).

At $t = 100$ s, the vehicle is accelerated to 22 mph (Fig. 4a), and a maximum temperature of 302 K (28 °C) is achieved in the core of the cell. When the vehicle is accelerated to the highest speed of 58 mph ($t = 200$ s), the maximum temperature achieved within the cell is 320 K (47 °C). However, from Fig. 6a it can be noted that the average temperature of the cell remains below 313 K (40 °C), so the cell fully operates within an optimal range of operating temperature estimated for LIBs [56]. At $t = 260$ s and $t = 360$ s the vehicle is accelerated to 38 mph and 30 mph respectively, corresponding to an average temperature of 305 K (32 °C) and 309 K (36 °C). In addition, it can be noted that for a low and moderate current demand the maximum temperature is located in the separator region since the main contribution to the heat losses is given by the ohmic resistance of the electrolyte. On the other hand, with an increase in current demand, the main contribution to the heat losses

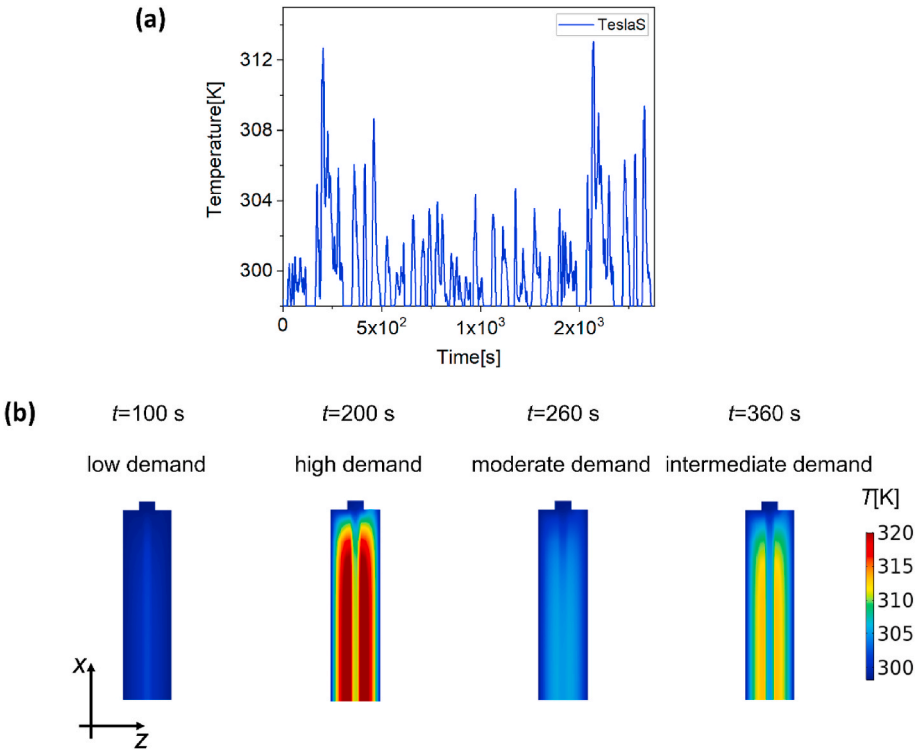

Fig. 6. (a) Temperature variation during the first repetition of the FTP75 DC of the cylindrical NMC cell together with **(b)** the bulk temperature distribution for four time-steps corresponding to the different levels of current demand during driving.

is given by the irreversible term due to the electrochemical reactions within the electrodes, so the maximum temperature is located in the electrode's region. Our approach allows us to provide the data of the fluctuating temperature within the cell, which is more informative than just the temperature of the surface which remains more or less constant during the discharge of the cell.

3.2. Battery degradation

In this section, the analysis of the capacity fade due to the battery degradation is presented. In particular, the growth of the SEI thickness and the SOH are investigated. Different DCs are applied to discharge a battery, while charging is performed at 1 C-rate. Among different aging mechanisms, the SEI film formation is one of the most harmful sources of loss of cyclable lithium in LIBs [57,58]. Such a passivation layer prevents further decomposition of the electrolyte by blocking the electron transfer and exfoliation of the graphite in the negative electrode, but it could be also the source of undesired phenomena such as anisotropic diffusivity of the Lithium ions to the electrode surface [59] which limits the performance of the battery and causes a potential failure. The formation of the SEI begins at the first charge cycle of the battery, and it continues to evolve during cycling, with a growth of the thickness from few nm to tens of nm. The SEI behavior is also highly dependent on the operating temperature of the cell, in particular at high temperatures for which the transformation of certain components and reaction with the electrolyte or active material occurs.

We report here the results obtained by simulating 2000 repetitions of a full charge-discharge life cycle (corresponding approximately to two years of operation) using the degradation electrochemical model of LIBs reported in section *2.2*. The simulation is performed considering the ambient temperature of 298K (25 °C). The purpose of this study is to investigate the growth of SEI in the cylindrical NMC cell of Tesla S and in the pouch LMO cell of Nissan Leaf subjected to a discharging current corresponding to the BEV operation. The calculation of the thickness of the SEI layer and the SOH are implemented according to the mathematical model for SEI formation reported in Ref. [52]. In particular, the SEI thickness and the SOH are related to qSEI, the capacity loss as a result of the side reactions generating the SEI. The charging of the cell is simulated at a constant current of 1C, while the discharge is modeled considering the discharging current for the FTP75 DC.

During the first charge-discharge cycle, the SEI grows up to around 0.014 nm (Fig. 7a), whereas an expansion up to around 30 nm is observed after 2000 cycles (Fig. 7b). Also, in Fig. 7a it could be noted that during charging at 1C, a steeper growth of the SEI is observed compared to the charging at low C-rates, which is induced by the recuperation current of the FTP75 protocol. The degradation of the battery over 2000 cycles due to SEI leads to a decay of the SOH up to 14% (Fig. 7c), meaning that the battery pack need to be replaced after this operation period. The values of the SEI thickness and the SOH shown in Fig. 7b and **c** correspond to values at the end of a complete charge-discharge cycle, like the one reported in Fig. 7a. Since the growth of the SEI and the capacity loss are approximately constant in each cycle, the variations of the values of the SEI thickness and SOH at end of each cycle exhibit a linear behavior. These profiles should not be confused with temporal variation during each cycle, which are indeed non-linear as shown in Fig. 7a. The degradation due to SEI is slightly higher for Tesla S compared to Nissan Leaf. Such small discrepancy is due to the different chemistry charactering the battery packs of the two vehicles.

3.3. Data preprocessing

The simulated data obtained with the modeling approach discussed

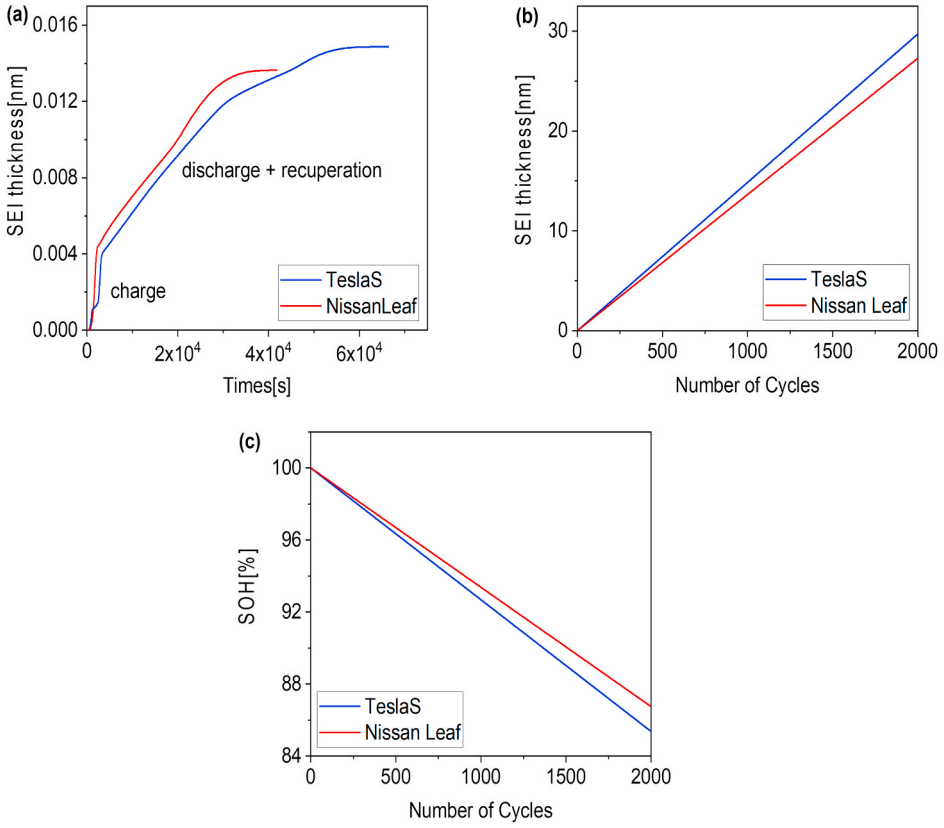

Fig. 7. Simulation of battery degradation for 2000 repetitions of charge-discharge life cycles (2 years of operation) for the FTP75 DC. **(a)** Growth of the SEI film during the first cycle of discharge. **(b)** Growth of the SEI thickness and **(c)** SOH decay over the 2000 life cycles. For each of the 2000 cycles, the values at the end of the discharge cycle are reported.

in the previous section need to be preprocessed in an appropriate manner before being fed to ML models. In this section the methodology for the preparation of the training and test datasets is presented.

The BEV model of Tesla S can be simulated for more repetitions of the different driving cycles compared to Nissan Leaf, as it is shown in Fig. 4b. Thus, Tesla S datasets have almost the double number of data points compared to Nissan Leaf datasets. The higher size of the datasets could bias a data driven model to overfit the Tesla S configuration, resulting in lower predicting capabilities of the SOC for Nissan Leaf. In order to prevent this issue, the Tesla S datasets is filtered by a random and uniform removal of datapoints until the datasets have an equal number of samples. Then, each variable is scaled using a Gaussian scaler, which performs a standardization to a null mean and unit variance. Features scaling is a well-established technique in statistics, which has been proven to be beneficial in the application of ML and DL models

$$\bar{x} = \frac{x - u}{s} \tag{4}$$

Equation (4) describes the Gaussian standardization, where to the feature x is removed its mean value u and the result is divided by the standard deviation s.

Different approaches could be used to create the training and validation datasets from the simulated data characterizing the six driving cycles for the Tesla S and Nissan Leaf. An approach could be to combine all the twelve datasets and randomly split 70% of the data for training and 30% for test (these are the percentages typically considered to pick the training and test datasets in ML). A second approach could be to use the first 70% of the total repetitions of the driving cycles for training and the last 30% for the test. Compared to the previous case, this approach allows to preserve the temporal evolution in the training and test datasets. A third approach is to select certain DCs for training and completely different DCs for the validation. A fourth and similar approach applied to our proposed modeling datasets is to use the simulated data of Tesla S for training and Nissan Leaf data for test (or vice-versa). Compared to the first two methods, the third and fourth methods are useful to evaluate the extrapolation capabilities of the models, since distinct configurations in terms of DCs and BEVs are used for training and test. In particular, the fourth method allows to investigate if a data driven model can extrapolate in the case of a different chemistry of the battery pack, which to our knowledge is a task still not addressed in the prior literature.

In this work, we first adopt distinct DCs to create the training and test datasets (**Case 1**). US06, HDUDDS, SC03 and LA92 are used for training, while FTP75 and HWFET are considered for test. It should be noted that there is not a particular reason behind the choice of the specific DC to use for the training and test datasets, and the same analysis could be performed by selecting other DCs' combinations. Then, we employ the Tesla S simulated data for training and the Nissan Leaf simulated date for test (**Case 2**). The formation of the training and test datasets is summarized in Table 1.

Table 1
Two different methods to create the training and test datasets from the twelve simulated datasets of the Tesla S (TS) and Nissan Leaf (NL) models.

Simulated Dataset	Case 1	Case 2
FTP75 TS	Test	Training
FTP75 NL	Test	Test
US06 TS	Training	Training
US06 NL	Training	Test
HWFET TS	Test	Training
HWFET NL	Test	Test
HDUDDS TS	Training	Training
HDUDDS NL	Training	Test
SC03 TS	Training	Training
SC03 NL	Training	Test
LA92 TS	Training	Training
LA92 NL	Training	Test

3.4. State-of-charge estimation

Here, we present the results of the estimation of the SOC using the considered learning algorithms applied to the datasets created with our proposed modeling framework. Through a 10-fold cross-validation it is found that the optimal configuration of the SVR is reported using a linear kernel with values of the regularization parameter C and the slack variable ξ equal to 0.1. Similarly, the ANN built using a single hidden layer comprising 128 neurons and trained for 500 epochs using a batch size of 32 samples provides the most accurate SOC estimation. Finally, for the LSTM network, 512 are used for the hidden states and a time sequence length l of 500 time-steps is employed. Usually, increasing the depth in time of the input time sequence reduces the error in the target estimation. For instance, Chemali et al. [35] found that for their LSTM, increasing the length of the time sequence from 250 to 500 leads to a reduction of the mean absolute error (MAE) by a half, but moving from 500 to 1000, provides only a 15% of the mean absolute error (MAE). The LSTM is trained for 200 epochs. It should be noted that similar as in any deep learning analysis, the values of the hyperparameters are always a trade-off between the performance, the number of epochs required for the training and the computational time.

Fig. 8a–c shows that for **Case 1**, all the models have satisfactory extrapolation capabilities when predicting the SOC for the FTP75 driving cycle which is not included in the training dataset. The less accurate estimation is reported by the SVR (MSE = 1.639 for Tesla S and MSE = 1.319 for Nissan Leaf), while ANN (MSE = 0.045 for Tesla S and MSE = 0.033 for Nissan Leaf) and LSTM (MSE = 0.082 for Tesla S and MSE = 0.064 for Nissan Leaf) exhibit similar performances. Table 2 reports the values of the MSE for the entire training dataset and test datasets built for **Case 1**.

The analysis for **Case 2** highlights if the models can extrapolate in the case of a different chemistry characterizing the battery pack and the different technical characteristics of the vehicles such as the electric motor and the powertrain system. For the sake of comparison with **Case 1**, the value of the hyperparameters of the models and the architectures of the ANN and LSTM are not changed. Fig. 8-*d*-e-f reveal that the test MSE of Nissan Leaf is higher than the training MSE of Tesla S for all the three models. In the zooming box on the first FTP75 cycle, it can be noted an accurate fitting for Tesla S while there is remarkable divergence between the estimated and the true profiles for Nissan Leaf. This is particularly evident for SVR, which provides a high MSE value also for the training data of Tesla S. Table 3 reports the training and test results obtained for the whole training and test datasets. For all the three models, it can be noted that the test MSE obtained on Nissan Leaf data is higher than the training MSE obtained on Tesla S data by two orders of magnitude. Overall, the extrapolation on Nissan Leaf dataset is still satisfactory; however, it is much less accurate than Tesla S compared to the results obtained with the datasets of **Case 1**.

The analysis reported in **Case 2** remarks the importance of considering different chemistries in the training of a data driven model, since a model trained on a particular chemistry is not able to perform with the same level of accuracy on a different chemistry.

4. Summary and conclusions

In this work, a computational study of LIBs SOC estimation in BEV combining automotive simulations, electrochemical-degradation-thermal modeling of battery and ML algorithms is presented. The test cases are the battery packs from Tesla S and Nissan Leaf models currently available in the BEV market. The automotive simulations performed for six EPA DCs, (i.e., FTP75, US06, HWFET, HDUDDS, SCO3 and LA92) have allowed us to simulate the variation of the discharging current flowing in the NMC cylindrical cells of Tesla S and LMO pouch cells of Nissan Leaf battery packs, as well as of the variables related to the powertrain system. The consistency of our proposed automotive modeling is demonstrated by the full discharge of the battery pack

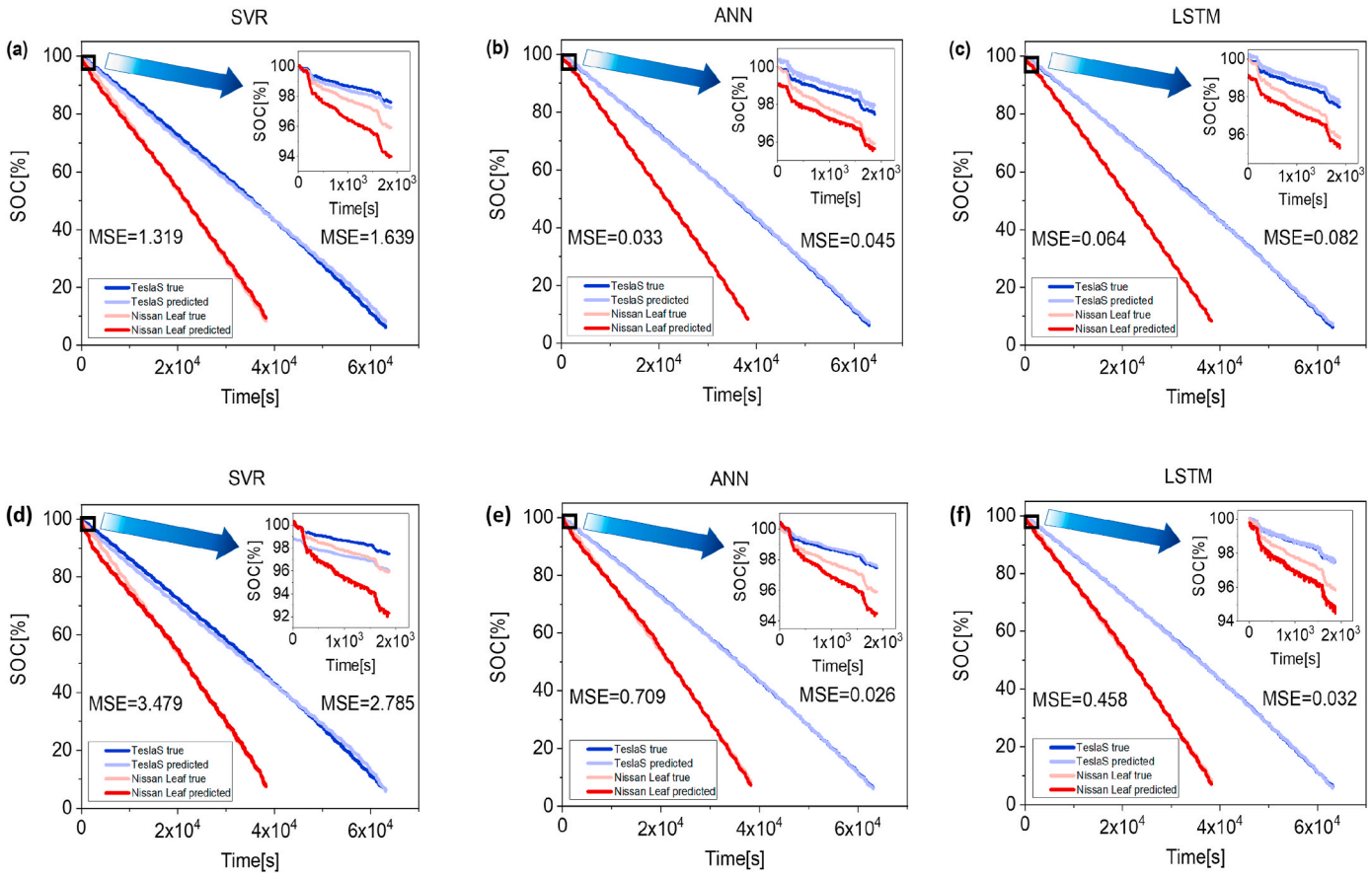

Fig. 8. SOC estimation for the FTP75 driving cycles obtained by training and testing the models on the datasets created by DC selection (**Case 1**). Prediction of the SOC for Tesla S (blue color) and Nissan Leaf (red color) using **(a)** SVR, **(b)** ANN, and **(c)** LSTM. SOC estimation for the FTP75 driving cycles obtained by training and testing the models on the datasets created by BEV selection (**Case 2**). Prediction of the SOC for Tesla S and Nissan Leaf using **(d)** SVR, **(e)** ANN, and **(f)** LSTM. (For interpretation of the references to color in this figure legend, the reader is referred to the Web version of this article.)

Table 2
Values of the training and test MSE reported by the SVR and ANN for the whole training and test datasets created by DC selection (**Case 1**).

Model	Training MSE	Test MSE
SVR	1.963×10^{-3}	2.038×10^{-3}
ANN	3.379×10^{-5}	1.191×10^{-4}
LSTM	7.748×10^{-4}	7.653×10^{-4}

Table 3
Values of the training and test MSE reported by the SVR and ANN for the whole training and test datasets created by BEV selection (**Case 2**).

Model	Training MSE	Test MSE
SVR	3.535×10^{-3}	5.636×10^{-1}
ANN	7.615×10^{-5}	1.031×10^{-3}
LSTM	7.959×10^{-5}	1.397×10^{-3}

corresponding to the driving range estimated by EPA for Tesla S and Nissan Leaf. The simulated current is used to model the thermal behavior and the degradation of the battery during the operation of the vehicle using the developed electrochemical model. This work is mainly focused on the Tesla S and Nissan Leaf models which employ NMC and LMO cells respectively; however, the proposed modeling framework is amenable to other types of BEVs characterized by different chemistries. Applications of such different chemistries will be considered in future publications.

The results of the computed temperature distribution within a cell match with the operating window recognized for BEV operation, serving as a further validation of our coupled automotive-electrochemical model. A capacity loss around 14% due to degradation (i.e., the growth of the SEI) is simulated for a life-cycle corresponding to two years of operation, which is a realistic estimation compared to the practical aging conditions. Although our model is capable of reproducing a realistic capacity loss profile due to the SEI formation/decomposition, such models require detail material information, which are rarely available for commercial cells. Thus, there is a necessity to experimentally measure such properties, which could improve the prediction of our model. Next, the modeling data reflecting real-life behavior of BEVs, have been employed to train and test an SVR, an ANN and an LSTM networks for the prediction of the SOC.

Compared to the attempts reported in the prior literature, a focus of this work is to feed ML models with more realistic data characterizing the BEV operation compared to the experimental data collected through discharge tests of a cell performed in a laboratory. A second goal is to allow a data driven model to capture the relationships between the SOC and variables related to the vehicle's dynamics, such as the mechanical power in the powertrain system and the aerodynamic resistance of the wind, in addition to the cell variables (i.e., current, voltage and temperature) adopted in the prior literature. As a first case, we have considered the extrapolation in the SOC estimation by training the models on selected driving cycles and testing on other unseen driving cycles. Then, we have investigated a second extrapolation case where the Tesla S data have been used for training while Nissan Leaf data have been used for test. Overall, the adopted models offer a satisfactory estimation of the SOC, where a more precise prediction is observed by

ANN and LSTM compared to SVR. Comparing the two cases, it has been found that a more precise extrapolation is obtained by applying the models on unseen driving cycles compared to an unseen BEV. This finding indicates that an accurate SOC estimation using data driven approaches has to be supported by the retrieval of training data comprehensive enough of different BEV configurations, which is the primary objective of this work. Although this report is mainly focused on the estimation of the battery's SOC, the proposed multi-physics modeling framework for the generation of realistic training data could be extended to the boosting of ML models in other applications of interest in BEV's research, such as the impact of the driving conditions on the triggering of thermal runaway or on the internal chemistry of battery pack.

CRediT authorship contribution statement

Marco Ragone: Methodology, Investigation, Formal analysis, Software, Validation, Visualization, Writing - original draft. **Vitaliy Yurkiv:** Supervision, Resources, Writing - review & editing. **Ajaykrishna Ramasubramanian:** Writing - review & editing. **Babak Kashir:** Writing - review & editing. **Farzad Mashayek:** Project administration, Supervision, Resources, Writing - review & editing.

Declaration of competing interest

The authors declare that they have no known competing financial interests or personal relationships that could have appeared to influence the work reported in this paper.

Acknowledgments

The authors acknowledge the financial support from the National Science Foundation, award CBET-1805938, as well as CNS-1828265. Lance Long (Electronic Visualization Laboratory, UIC) is gratefully acknowledged for helping with running machine learning calculations on GPU cluster.

Appendix A. Supplementary data

Supplementary data related to this article can be found at https://doi.org/10.1016/j.jpowsour.2020.229108.

References

[1] B.M. Al-Alawi, T.H. Bradley, Review of hybrid, plug-in hybrid, and electric vehicle market modeling Studies, Renew. Sustain. Energy Rev. 21 (2013) 190–203, https://doi.org/10.1016/j.rser.2012.12.048.
[2] A.F. Burke, Batteries and ultracapacitors for electric, hybrid, and fuel cell vehicles, Proc. IEEE 95 (2007) 806–820, https://doi.org/10.1109/JPROC.2007.892490.
[3] P. Kurzweil, Post-lithium-ion Battery Chemistries for Hybrid Electric Vehicles and Battery Electric Vehicles, 2015, https://doi.org/10.1016/B978-1-78242-377-5.00007-8.
[4] J.W. Choi, D. Aurbach, Promise and reality of post-lithium-ion batteries with high energy densities, Nat. Rev. Mater. 1 (2016), https://doi.org/10.1038/natrevmats.2016.13.
[5] Y. Xing, E.W.M. Ma, K.L. Tsui, M. Pecht, Battery management systems in electric and hybrid vehicles, Energies 4 (2011) 1840–1857, https://doi.org/10.3390/en4111840.
[6] M.A. Hannan, M.S.H. Lipu, A. Hussain, A. Mohamed, A review of lithium-ion battery state of charge estimation and management system in electric vehicle applications: challenges and recommendations, Renew. Sustain. Energy Rev. 78 (2017) 834–854, https://doi.org/10.1016/j.rser.2017.05.001.
[7] D.N.T. How, M.A. Hannan, M.S. Hossain Lipu, P.J. Ker, State of charge estimation for lithium-ion batteries using model-based and data-driven methods: a review, IEEE Access 7 (2019) 136116–136136, https://doi.org/10.1109/ACCESS.2019.2942213.
[8] R. Xiong, J. Cao, Q. Yu, H. He, F. Sun, Critical review on the battery state of charge estimation methods for electric vehicles, IEEE Access 6 (2017) 1832–1843, https://doi.org/10.1109/ACCESS.2017.2780258.
[9] I. Snihir, W. Rey, E. Verbitskiy, A. Belfadhel-Ayeb, P.H.L. Notten, Battery open-circuit voltage estimation by a method of statistical analysis, J. Power Sources 159 (2006) 1484–1487, https://doi.org/10.1016/j.jpowsour.2005.11.090.
[10] W. Waag, D.U. Sauer, Adaptive estimation of the electromotive force of the lithium-ion battery after current interruption for an accurate state-of-charge and capacity determination, Appl. Energy 111 (2013) 416–427, https://doi.org/10.1016/j.apenergy.2013.05.001.
[11] Y.P. Yang, J.J. Liu, C.H. Tsai, Improved estimation of residual capacity of batteries for electric vehicles, J. Chinese Inst. Eng. Trans. Chinese Inst. Eng. A/Chung-Kuo K. Ch'eng Hsuch K'an. 31 (2008) 313–322, https://doi.org/10.1080/02533839.2008.9671384.
[12] L. Lu, X. Han, J. Li, J. Hua, M. Ouyang, A review on the key issues for lithium-ion battery management in electric vehicles, J. Power Sources 226 (2013) 272–288, https://doi.org/10.1016/j.jpowsour.2012.10.060.
[13] A. Hentunen, T. Lehmuspelto, J. Suomela, Time-domain parameter extraction method for thévenin-equivalent circuit battery models, IEEE Trans. Energy Convers. 29 (2014) 558–566, https://doi.org/10.1109/TEC.2014.2318205.
[14] R. Ahmed, M. El Sayed, I. Arasaratnam, J. Tjong, S. Habibi, Reduced-order electrochemical model parameters identification and state of charge estimation for healthy and aged Li-ion batteries—Part II: aged battery model and state of charge estimation, IEEE J. Emerg. Sel. Top. Power Electron. 2 (2014) 678–690, https://doi.org/10.1109/jestpe.2014.2331062.
[15] T.O. Ting, K.L. Man, N. Zhang, C.U. Lei, C. Lu, State-space battery modeling for smart battery management system, Lect. Notes Eng. Comput. Sci. 2210 (2014) 12–15.
[16] K.A. Smith, C.D. Rahn, C.Y. Wang, Model-based electrochemical estimation and constraint management for pulse operation of lithium ion batteries, IEEE Trans. Contr. Syst. Technol. 18 (2010) 654–663, https://doi.org/10.1109/TCST.2009.2027023.
[17] M. Li, Li-ion dynamics and state of charge estimation, Renew. Energy 100 (2017) 44–52, https://doi.org/10.1016/j.renene.2016.06.009.
[18] T.O. Ting, K.L. Man, E.G. Lim, M. Leach, Tuning of Kalman filter parameters via genetic algorithm for state-of-charge estimation in battery management system, Sci. World J. 2014 (2014), https://doi.org/10.1155/2014/176052.
[19] Z. Chen, Y. Fu, C.C. Mi, State of charge estimation of lithium-ion batteries in electric drive vehicles using extended Kalman filtering, IEEE Trans. Veh. Technol. 62 (2013) 1020–1030, https://doi.org/10.1109/TVT.2012.2235474.
[20] W. He, N. Williard, C. Chen, M. Pecht, State of charge estimation for electric vehicle batteries using unscented kalman filtering, Microelectron. Reliab. 53 (2013) 840–847, https://doi.org/10.1016/j.microrel.2012.11.010.
[21] F. Sun, X. Hu, Y. Zou, S. Li, Adaptive unscented Kalman filtering for state of charge estimation of a lithium-ion battery for electric vehicles, Energy 36 (2011) 3531–3540, https://doi.org/10.1016/j.energy.2011.03.059.
[22] I.S. Kim, Nonlinear state of charge estimator for hybrid electric vehicle battery, IEEE Trans. Power Electron. 23 (2008) 2027–2034, https://doi.org/10.1109/TPEL.2008.924629.
[23] L. Wang, L. Wang, Y. Li, A novel state-of-charge estimation algorithm of ev battery based on bilinear interpolation, 2013 9th IEEE Veh, Power Propuls. Conf. IEEE VPPC (2013) (2013) 26–29, https://doi.org/10.1109/VPPC.2013.6671658.
[24] S. Malkhandi, Fuzzy logic-based learning system and estimation of state-of-charge of lead-acid battery, Eng. Appl. Artif. Intell. 19 (2006) 479–485, https://doi.org/10.1016/j.engappai.2005.12.005.
[25] Y. Zheng, L. Lu, X. Han, J. Li, M. Ouyang, LiFePO4 battery pack capacity estimation for electric vehicles based on charging cell voltage curve transformation, J. Power Sources 226 (2013) 33–41, https://doi.org/10.1016/j.jpowsour.2012.10.057.
[26] J.C. Álvarez Antón, P.J. García Nieto, F.J. de Cos Juez, F. Sánchez Lasheras, M. González Vega, M.N. Roqueñí Gutiérrez, Battery state-of-charge estimator using the SVM technique, Appl. Math. Model. 37 (2013) 6244–6253, https://doi.org/10.1016/j.apm.2013.01.024.
[27] C. Hu, G. Jain, C. Schmidt, C. Strief, M. Sullivan, Online estimation of lithium-ion battery capacity using sparse Bayesian learning, J. Power Sources 289 (2015) 105–113, https://doi.org/10.1016/j.jpowsour.2015.04.166.
[28] C. Bo, B. Zhifeng, C. Binggang, State of charge estimation based on evolutionary neural network, Energy Convers. Manag. 49 (2008) 2788–2794, https://doi.org/10.1016/j.enconman.2008.03.013.
[29] L.W. Kang, X. Zhao, J. Ma, A new neural network model for the state-of-charge estimation in the battery degradation process, Appl. Energy 121 (2014) 20–27, https://doi.org/10.1016/j.apenergy.2014.01.066.
[30] T. Zahid, K. Xu, W. Li, C. Li, H. Li, State of charge estimation for electric vehicle power battery using advanced machine learning algorithm under diversified drive cycles, Energy 162 (2018) 871–882, https://doi.org/10.1016/j.energy.2018.08.071.
[31] S. Tong, J.H. Lacap, J.W. Park, Battery state of charge estimation using a load-classifying neural network, J. Energy Storage. 7 (2016) 236–243, https://doi.org/10.1016/j.est.2016.07.002.
[32] M.A. Hannan, M.S.H. Lipu, A. Hussain, M.H. Saad, A. Ayob, Neural network approach for estimating state of charge of lithium-ion battery using backtracking search algorithm, IEEE Access 6 (2018) 10069–10079, https://doi.org/10.1109/ACCESS.2018.2797976.
[33] E. Chemali, P.J. Kollmeyer, M. Preindl, A. Emadi, State-of-charge estimation of Li-ion batteries using deep neural networks: a machine learning approach, J. Power Sources 400 (2018) 242–255, https://doi.org/10.1016/j.jpowsour.2018.06.104.
[34] H. Pan, Z. Lü, H. Wang, H. Wei, L. Chen, Novel battery state-of-health online estimation method using multiple health indicators and an extreme learning machine, Energy 160 (2018) 466–477, https://doi.org/10.1016/j.energy.2018.06.220.
[35] E. Chemali, P.J. Kollmeyer, M. Preindl, R. Ahmed, A. Emadi, Long short-term memory networks for accurate state-of-charge estimation of Li-ion batteries, IEEE

Trans. Ind. Electron. 65 (2018) 6730–6739, https://doi.org/10.1109/TIE.2017.2787586.
[36] Tesla Home Page: https://www.tesla.com/models, (n.d.).
[37] Nissan Leaf Home Page: https://www.nissanusa.com/vehicles/electric-cars/leaf.html,(n.d.).
[38] D.R.Z. Aaron Brooker, Kristina Haraldsson, Hendricks Terry, Valerie Johnson, Kenneth Kelly, Bill Kramer, Tony Markel, Michael O'Keefe, Sprik Sam, Wipke Keith, Desikan Bharathan Matthew, Steve Burch, Matthew Cuddy, ADVISOR Documentation. March 26, 2013. Available from: http://adv-vehicle-sim.sourceforge.net/advisor_doc.html, 2013.
[39] MATLAB and Simulink Release 2019b, The MathWorks, Inc., Natick, Massachusetts, United States., (n.d.).
[40] MATLAB and Powertrain Blockset Toolbox Release 2019b, The MathWorks, Inc., Natick, Massachusetts, United States., (n.d.).
[41] Comsol Multiphysics® v. 5.5. www.comsol.com. COMSOL AB, Stockholm, Sweden.,(n.d.).
[42] É.D. Fabian Pedregosa, Gaël Varoquaux, Alexandre Gramfort, Vincent Michel, Thirion Bertrand, Olivier Grisel, Mathieu Blondel, Prettenhofer Peter, Ron Weiss, Vincent Dubourg, Jake Vanderplas, alexandre Passos, David Cournapeau, Matthieu Brucher, Matthieu Perrot, Scikit-learn: machine learning in Python, GetMobile Mob. Comput. Commun. 12 (2011) 2825–2830, https://doi.org/10.1145/2786984.2786995.
[43] M. Abadi, A. Agarwal, P. Barham, E. Brevdo, Z. Chen, C. Citro, G.S. Corrado, A. Davis, J. Dean, M. Devin, S. Ghemawat, I. Goodfellow, A. Harp, G. Irving, M. Isard, Y. Jia, R. Jozefowicz, L. Kaiser, M. Kudlur, J. Levenberg, D. Mane, R. Monga, S. Moore, D. Murray, C. Olah, M. Schuster, J. Shlens, B. Steiner, I. Sutskever, K. Talwar, P. Tucker, V. Vanhoucke, V. Vasudevan, F. Viegas, O. Vinyals, P. Warden, M. Wattenberg, M. Wicke, Y. Yu, X. Zheng, TensorFlow: Large-Scale Machine Learning on Heterogeneous Distributed Systems, ArXiv, 2016.
[44] U.S. MATLAB and Battery Datasheet Block Release 2019b, The MathWorks, Inc., Natick, Massachusetts, https://www.mathworks.com/help/autoblks/ref/datasheetbattery.html, (n.d.).
[45] U.S. MATLAB and Mapped Motor Block Release 2019b, The MathWorks, Inc., Natick, Massachusetts, https://www.mathworks.com/help/autoblks/ref/mappedmotor.html, (n.d.).
[46] U.S. MATLAB and Limited Slip Differential Block Release 2019b, The MathWorks, Inc., Natick, Massachusetts, https://www.mathworks.com/help/autoblks/ref/limitedslipdifferential.html, (n.d.).
[47] U.S. MATLAB and Longitudinal Wheel Block Release 2019b, The MathWorks, Inc., Natick, Massachusetts, https://www.mathworks.com/help/autoblks/ref/longitudinalwheel.html, (n.d.).
[48] U.S. MATLAB and Vehicle Body 1DOF Longitudinal Block Release 2019b, The MathWorks, Inc., Natick, Massachusetts, https://www.mathworks.com/help/autoblks/ref/vehiclebody1doflongitudinal.html,(n.d.).
[49] M. Doyle, T. Fuller, J. Newman, Modeling of galvanostatic charge and discharge of the lithium/polymer/insertion cell, J. Electrochem. Soc. 140 (1993) 1526–1533, https://doi.org/10.1149/1.2221597.
[50] E. Peled, S. Menkin, Review—SEI: Past, present and future, J. Electrochem. Soc. 164 (2017) A1703–A1719, https://doi.org/10.1149/2.1441707jes.
[51] V. Yurkiv, T. Foroozan, A. Ramasubramanian, R. Shahbazian-Yassar, F. Mashayek, Phase-field modeling of solid electrolyte interface (SEI) influence on Li dendritic behavior, Electrochim. Acta 265 (2018) 609–619.
[52] H. Ekström, G. Lindbergh, A model for predicting capacity fade due to SEI formation in a commercial graphite/LiFePO 4 cell, J. Electrochem. Soc. 162 (2015) A1003–A1007, https://doi.org/10.1149/2.0641506jes.
[53] S. Abada, G. Marlair, A. Lecocq, M. Petit, V. Sauvant-Moynot, F. Huet, Safety focused modeling of lithium-ion batteries: a review, J. Power Sources 306 (2016) 178–192, https://doi.org/10.1016/j.jpowsour.2015.11.100.
[54] U.S. Kim, J. Yi, C.B. Shin, T. Han, S. Park, Modelling the thermal behaviour of a lithium-ion battery during charge, J. Power Sources 196 (2011) 5115–5121, https://doi.org/10.1016/j.jpowsour.2011.01.103.
[55] P. Taheri, M. Yazdanpour, M. Bahrami, Transient three-dimensional thermal model for batteries with thin electrodes, J. Power Sources 243 (2013) 280–289, https://doi.org/10.1016/j.jpowsour.2013.05.175.
[56] C. Zhao, W. Cao, T. Dong, F. Jiang, Thermal behavior study of discharging/charging cylindrical lithium-ion battery module cooled by channeled liquid flow, Int. J. Heat Mass Tran. 120 (2018) 751–762, https://doi.org/10.1016/j.ijheatmasstransfer.2017.12.083.
[57] N. Omar, Y. Firouz, H. Gualous, J. Salminen, T. Kallio, J.M. Timmermans, T. Coosemans, P. Van den Bossche, J. Van Mierlo, 9 - Aging and Degradation of Lithium-Ion Batteries, Elsevier Ltd., 2015, https://doi.org/10.1016/B978-1-78242-090-3.00009-2.
[58] P. Verma, P. Maire, P. Novák, A review of the features and analyses of the solid electrolyte interphase in Li-ion batteries, Electrochim. Acta 55 (2010) 6332–6341.
[59] A. Ramasubramanian, V. Yurkiv, T. Foroozan, M. Ragone, R. Shahbazian-Yassar, F. Mashayek, Lithium diffusion mechanism through solid-electrolyte interphase in rechargeable lithium batteries, J. Phys. Chem. C 123 (2019) 10237–10245, https://doi.org/10.1021/acs.jpcc.9b00436.